SUPPORTING INFORMATION

Unsupervised Machine Learning for Automated Crystal Orientation Mapping on Noisy 4D-STEM Data

Kai Kamijo[1], Motoki Shiga[1,2,3,4,*,†], Shusuke Kanomi[5,6], Tomohiro Miyata[5], and Hiroshi Jinnai[5]

*Corresponding author
†motoki.shiga.b4@tohoku.ac.jp

[1] Graduate School of Information Sciences, Tohoku University, 6-3-09 Aoba, Aramaki-aza Aoba-ku, Sendai, 980-8579, Japan

[2] Unprecedented-scale Data Analytics Center, Tohoku University, 468-1 Aramaki-Aza-Aoba, Aoba-ku, Sendai 980-8578, Japan

[3] Center for Basic Research on Materials, National Institute for Materials Science, 1-2-1, Sengen, Tsukuba, Ibaraki 305-0047, Japan

[4]RIKEN Center for Advanced Intelligence Project, 1-4-1 Nihonbashi, Chuo-ku, Tokyo 103-0027, Japan

[5]Institute of Multidisciplinary Research for Advanced Materials, Tohoku University, Katahira 2-1-1, Aoba-ku, Sendai 980-8577, Japan

[6]Science & Innovation Center, Mitsubishi Chemical Corporation, 1000 Kamoshida-cho, Aoba-ku, Yokohama-shi, Kanagawa, 227-8502, Japan

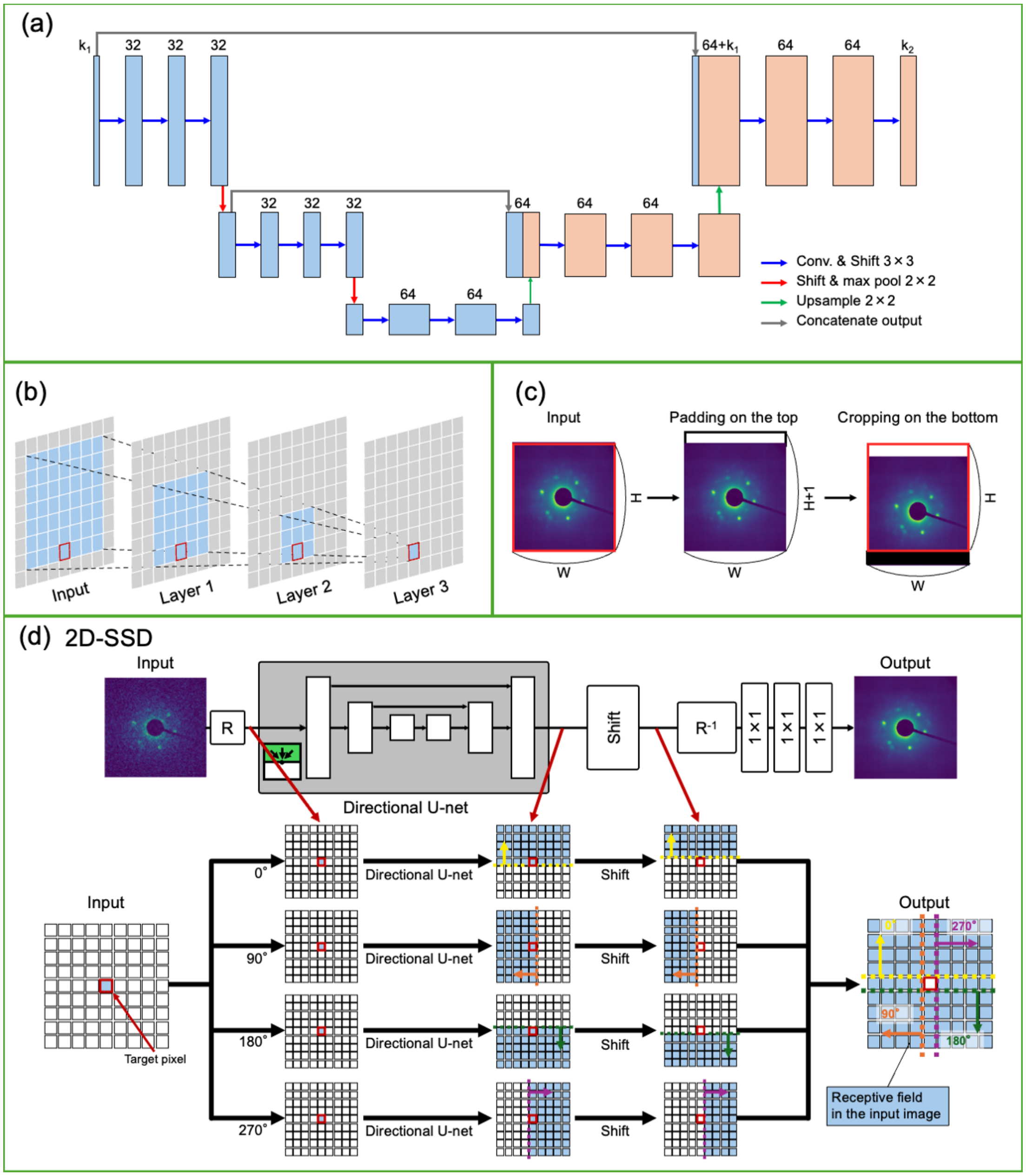

Supplementary Fig. 1. Blind-spot architecture based on 2D-SSD

(a) Architecture of the directional U-net. **(b)** Receptive field (blue regions) from the target pixel (the red rectangle) by two directional convolutions (convolution with a 3 × 3 kernel followed by upward-shift) as an example. This figure shows that the receptive field within the input is located at the same vertical positions or in the rows above the target position in the output. **(c)** Shift layer before the inverse-rotation operator denoted by R^{-1} in **Fig. 1b**. The feature maps are shifted by one pixel along the vertical direction by the combination of padding and cropping operations, thereby completely excluding the target pixel from the receptive field. **(d)** The receptive field of the target pixel (red square) in the input data. The fields are highlighted by blue regions. The target position was excluded in the field of the output, which is performed by the directional U-net and the shift operation.

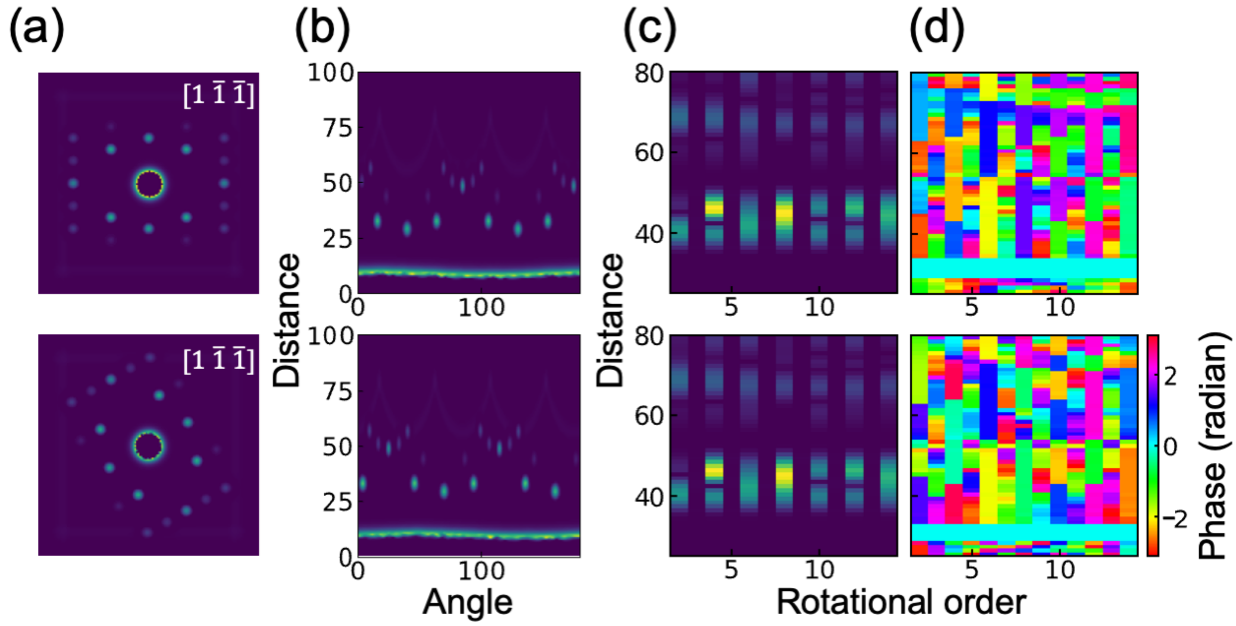

Supplementary Fig. 2. Data transformations of diffraction patterns from in-plane rotated crystals in component $[1\,\bar{1}\,\bar{1}]$.
(a) Diffraction patterns with rotational angles of $\theta = 0°$ (top) and $60°$ (bottom). **(b)** Polar representations of the diffraction patterns. **(c, d)** Magnitudes (c) and phases (d) of the Fourier transform of the polar representations.

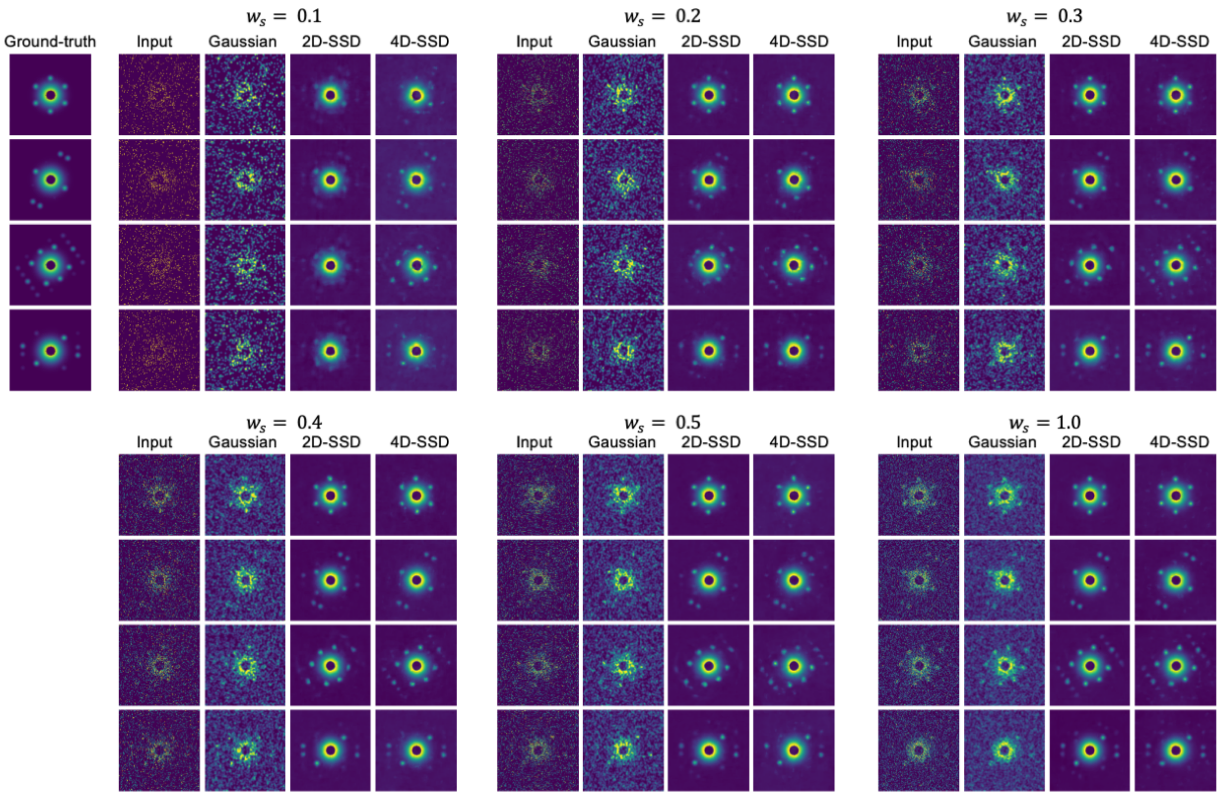

Supplementary Fig. 3. Examples of denoising results for synthetic data with various noise levels. The intensity range of each image was normalized for visualization. The parameter w_s refers to the S/N ratio in the synthetic 4D-STEM data and is inversely related to the noise level.

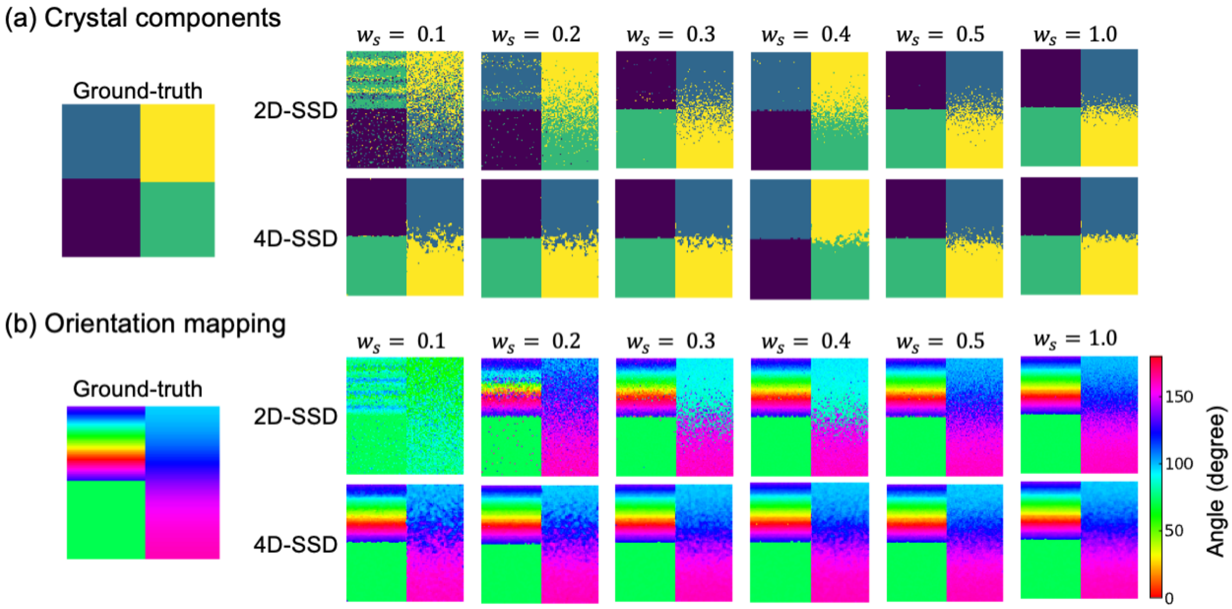

Supplementary Fig. 4. Crystallographic component analysis results for synthetic data with various noise levels.

(a) Spatial distributions of components denoised via 2D-SSD and 4D-SSD. For visualization, each position was assigned to a single component with the maximum intensity. **(b)** Spatial distributions of the in-plane rotational angles estimated from the Fourier phase images.

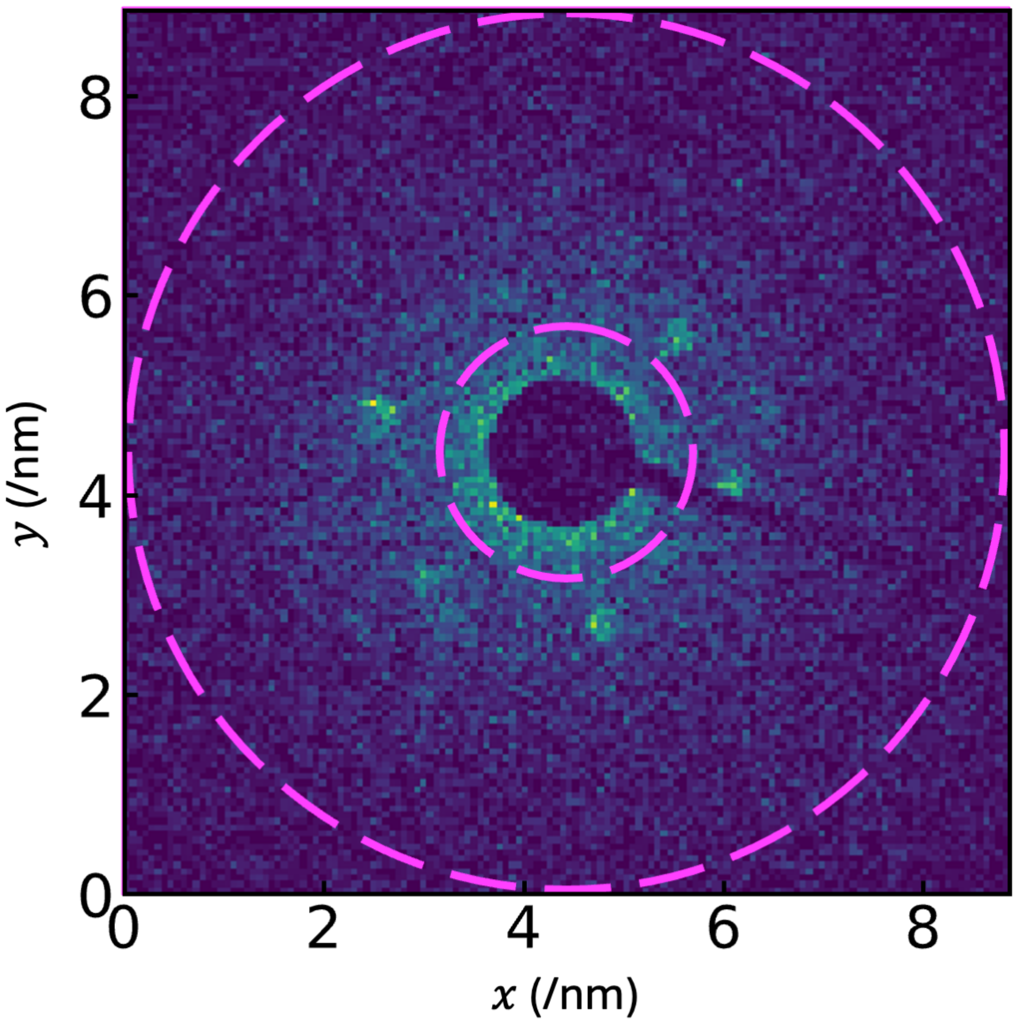

Supplementary Fig. 5. The annular range used for generating the ADF-STEM image (Fig. 6b) from the 4D-STEM data. The range is highlighted by the magenta dashed circles.

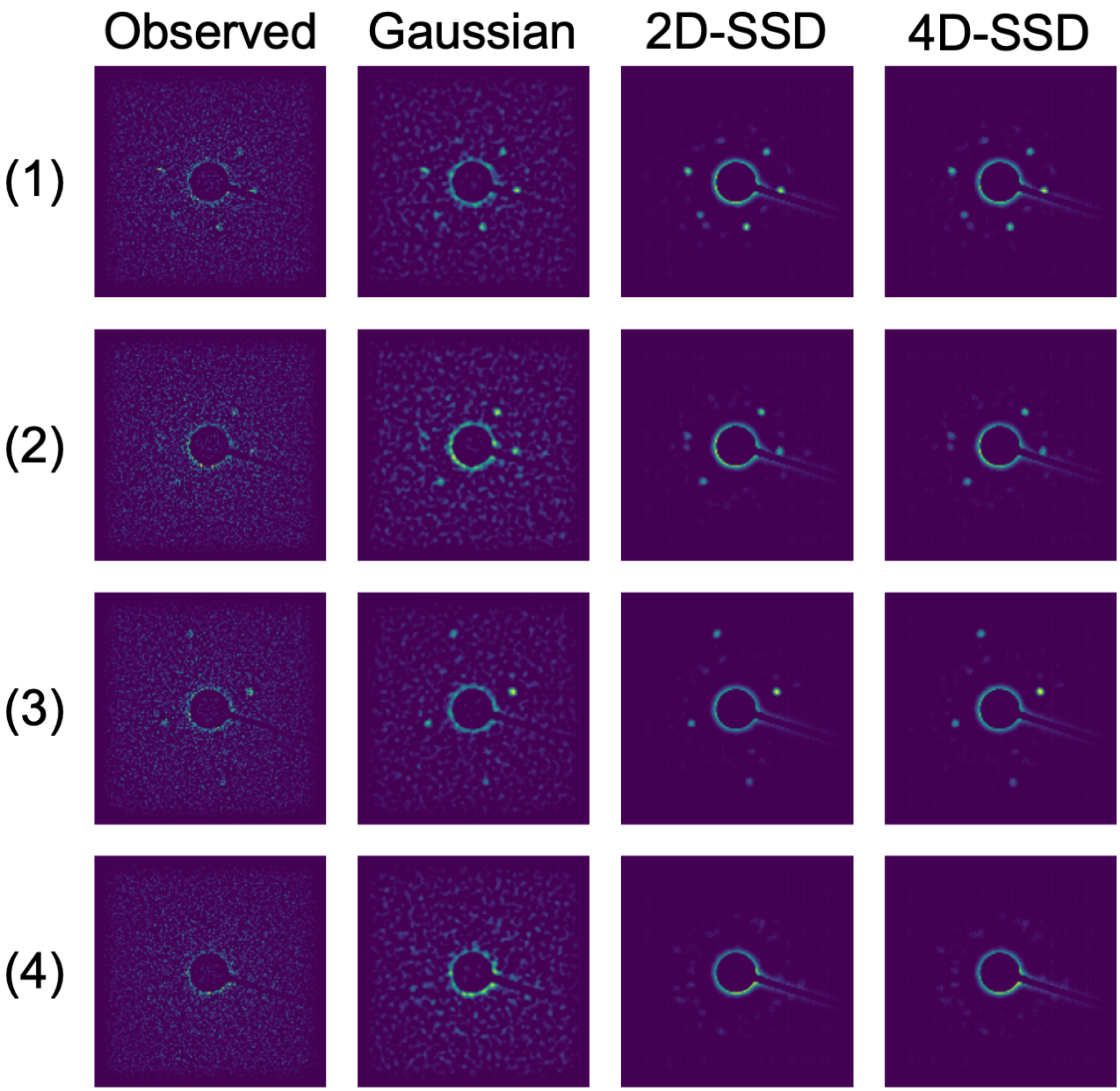

Supplementary Fig. 6. Diffraction patterns for experimental 4D-STEM data after denoising followed by the high-pass filtering.

Denoised images processed by a Gaussian filter, 2D-SSD, or 4D-SSD, followed by the high-pass filtering. Observation positions (1) – (4) are indicated in **Fig. 6b**.

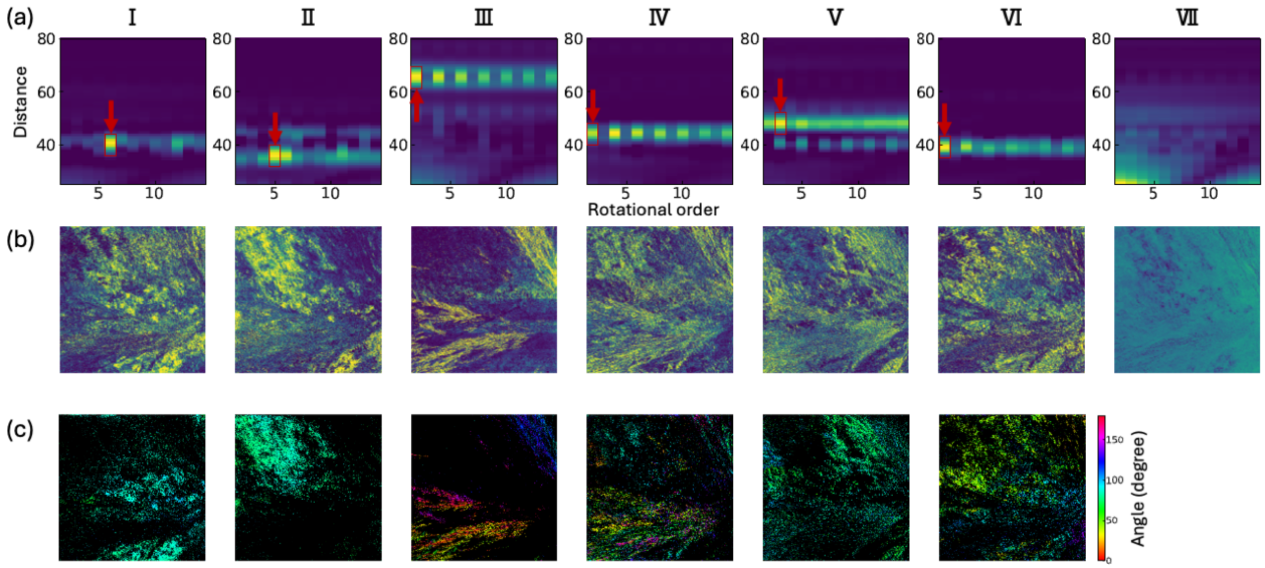

Supplementary Fig. 7. Crystal component analysis results obtained by NMF for real data

(a) Fourier magnitudes of the crystal components identified using NMF. **(b)** Spatial maps of the components. **(c)** Spatial map of the in-plane rotational angles estimated using our pipeline. The peak positions indicated by red arrows in (a) were used for angle estimation. The angles are displayed only in the map of the component where yields the maximum intensity at each position.

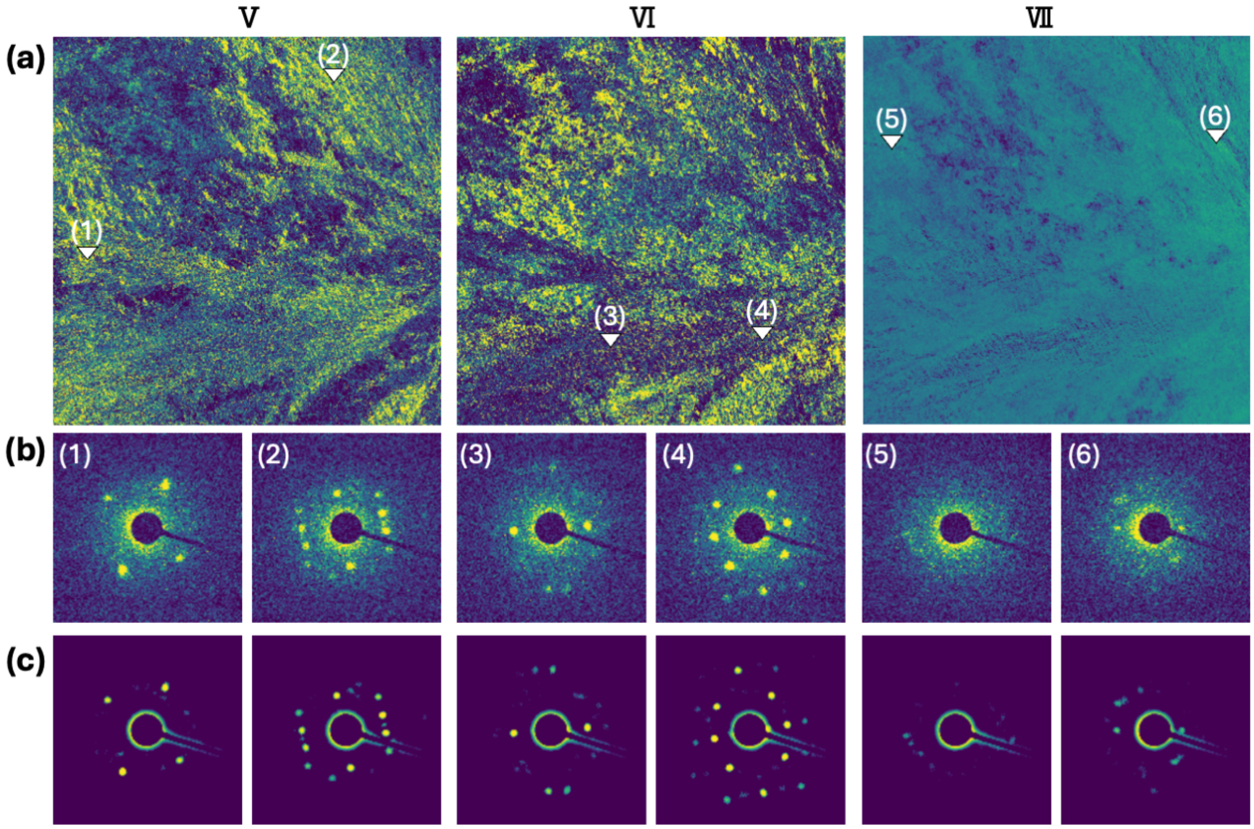

Supplementary Fig. 8. Spatial distribution of other components identified by NMF from real data

(a) Spatial distribution of components not identified as flat-on or edge-on lamellae. **(b)** Diffraction patterns observed at the positions indicated in the top panels. **(c)** Denoised diffraction patterns. The patterns were processed using the proposed denoising method, followed by high-pass filtering.

Supplementary Table 1. Denoising performance metrics for synthetic data with various S/N parameters w_s. The uPSNR of the ground-truth data for $w_s = 1.0$ was diverged because the uMSE was close to zero.

(a) PSNR [dB]

Name \ w_s	0.1	0.3	0.5	1.0
Observed	-4.07 ± 0.26	0.70 ± 0.10	2.92 ± 0.08	5.93 ± 0.07
Gaussian filter	9.79 ± 0.18	12.29 ± 0.13	13.87 ± 0.14	16.35 ± 0.13
2D-SSD	11.51 ± 0.24	15.04 ± 0.10	17.52 ± 0.12	21.58 ± 0.33
4D-SSD	11.65 ± 0.18	15.13 ± 0.17	17.35 ± 0.15	21.74 ± 0.24

(b) uPSNR [dB]

Name \ w_s	0.1	0.3	0.5	1.0
Ground-truth	41.53 ± 4.76	40.37 ± 4.72	43.73 ± 4.89	∞
Gaussian filter	5.93 ± 0.71	11.46 ± 0.54	14.17 ± 0.49	17.89 ± 0.50
2D-SSD	14.48 ± 3.96	18.04 ± 3.51	20.53 ± 3.36	24.64 ± 3.42
4D-SSD	14.64 ± 4.28	18.11 ± 3.51	20.41 ± 3.22	24.81 ± 3.72